

Microstructure and Residual Stress Evolution of Laser Powder Bed Fused Inconel 718 under Heat Treatments

*Original*

Microstructure and Residual Stress Evolution of Laser Powder Bed Fused Inconel 718 under Heat Treatments / Marchese, G.; Atzeni, E.; Salmi, A.; Biamino, S.. - In: JOURNAL OF MATERIALS ENGINEERING AND PERFORMANCE. - ISSN 1059-9495. - ELETTRONICO. - 30:1(2021), pp. 565-574. [10.1007/s11665-020-05338-z]

*Availability:*

This version is available at: 11583/2895903 since: 2021-04-20T12:16:12Z

*Publisher:*

Springer

*Published*

DOI:10.1007/s11665-020-05338-z

*Terms of use:*

This article is made available under terms and conditions as specified in the corresponding bibliographic description in the repository

*Publisher copyright*

(Article begins on next page)



# Microstructure and Residual Stress Evolution of Laser Powder Bed Fused Inconel 718 under Heat Treatments

Giulio Marchese, Eleonora Atzeni, Alessandro Salmi, and Sara Biamino

Submitted: 14 July 2020 / Revised: 13 October 2020 / Accepted: 7 November 2020 / Published online: 2 December 2020

**The current work aimed to study the influence of various heat treatments on the microstructure, hardness, and residual stresses of Inconel 718 processed by laser powder bed fusion process. The reduction in residual stresses is crucial to avoid the deformation of the component during its removal from the building platform. Among the different heat treatments, 800 °C kept almost unaltered the original microstructure, reducing the residual stresses. Heat treatments at 900, 980, and 1065 °C gradually triggered the melt pool and dendritic structures dissolution, drastically reducing the residual stresses. Heat treatments at 900 and 980 °C involved the formation of  $\delta$  phases, whereas 1065 °C generated carbides. These heat treatments were also performed on components with narrow internal channels revealing that heat treatments up to 900 °C did not trigger sintering mechanisms allowing to remove the powder from the inner channels.**

**Keywords** additive manufacturing, hardness, laser powder bed fusion, microstructure, phase state, residual stress, superalloys

## 1. Introduction

Inconel 718 (IN 718) is a Ni-based superalloy characterized by high mechanical stability up to around 650 °C, including elevated oxidation resistance and good fatigue life. This alloy is one of the most considered materials for aeronautics industries, such as parts of aircraft turbine engines and land-based gas turbine engines (Ref 1-7).

Nowadays, near-net-shape complex components made of IN 718 can be fabricated employing additive manufacturing (AM) processes. Among these processes, laser powder bed fusion (L-PBF) enables the production of components starting from powder melted by a laser beam layer by layer, based on a 3D CAD model (Ref 8-10). The high weldability of this alloy allows the fabrication of L-PBF IN 718 components with extremely high densification levels (close to 100%) (Ref 11-14).

However, the material is subjected to extremely high cooling rates (around  $10^5$ – $10^6$  °C/s) during the melting and solidification, generating extremely fine microstructures composed of dendritic/cellular structures with nanometric Laves phases, and micrometric segregations chiefly located into the interdendritic areas. Moreover, high cooling rates lead to the formation of high residual stresses within the material (Ref 11, 15-17). These high residual stresses can lead to distortion of the component as well as to reduce its fatigue life (Ref 18). It is

therefore essential to perform subsequent heat treatments in order to mitigate the residual stresses, investigating the microstructure and mechanical properties of the post-heat-treated material (Ref 17, 19, 20).

The primary studies on L-PBF IN 718 alloy have been investigated the effect of heat treatments (solution annealing and double-aging treatments) in order to homogenize the microstructure and reach adequate mechanical performance.

For instance, Tucho et al. (Ref 21) studied the effect of solution annealing at high temperatures (1100 and 1250 °C) for different times, showing the homogenization of the microstructure associated with its hardness evolution. Also, Calandri et al. (Ref 15) reported the crucial role of the chemical homogenization, investigating the phases concentration, grain structures, and hardness of L-PBF IN 718 underwent to different solution annealing from 980 to 1200 °C. Zhang et al. (Ref 22) focused their attention on the effect of standard heat treatments on the phases formation and hardness compared to the traditional cast version. Cao et al. (Ref 23) examined the evolution of the phases such as  $\gamma'$  ( $\text{Ni}_3(\text{Al,Ti})$ —face-centered cubic),  $\gamma''$  ( $\text{Ni}_3\text{Nb}$ —body-centered tetragonal) and  $\delta$  ( $\text{Ni}_3\text{Nb}$ —orthorhombic) phases under standard heat treatments. Chlebus et al. (Ref 24) reported that double-aged L-PBF IN 718 material exhibits higher tensile properties than double-aged wrought IN 718 alloy.

Another aspect of L-PBF process is that it inherently induces residual stresses into the material that can be determined by means of different techniques (Ref 18, 25-32). Regarding IN 718, some authors revealed an estimation based on the deformation of the specimens (Ref 28), microhardness test (Ref 29), XRD analysis (Ref 30), neutral diffraction method (Ref 31), as well as hole drilling test (Ref 32).

Yi et al. (Ref 28) reported the variations of residual stresses through the degree of sample deformations produced with different process parameters. They revealed that reducing the scanning speed or increasing the laser power involves more energy to the powder, thus provoking increment of residual stresses. Nadammal et al. (Ref 31) revealed the effect of parameters on the residual stresses assessed using the neutral diffraction method. Lu et al. (Ref 29) evaluated the influence of different island scanning strategies on the residual stresses by

**Giulio Marchese** and **Sara Biamino**, Department of Applied Science and Technology, Politecnico di Torino, Corso Duca degli Abruzzi 24, 10129 Turin, Italy; and **Eleonora Atzeni** and **Alessandro Salmi**, Department of Management and Production Engineering, Politecnico di Torino, Corso Duca degli Abruzzi 24, 10129 Turin, Italy. Contact e-mail: giulio.marchese@polito.it.

means of microhardness test, indicating an adequate reduction for the size of  $5 \times 5 \text{ mm}^2$ . Ahmad et al. (Ref 33) used the contour method (within the techniques based on the deformation of the sample) coupled with numerical simulation to determine the residual stresses generated within L-PBF IN 718. They assessed high tensile stresses (maximum values around 840 MPa) close to the surface and compressive stresses (maximum values around 460 MPa) in the middle of the specimens. Deng et al. (Ref 30) found high residual stresses for the as-built state (magnitude around 800–750 MPa), which are relieved after performing heat treatment at 1080 °C followed by double-aging treatments by means of XRD analysis. Finally, Barros et al. (Ref 32) studied the effect of residual stresses for L-PBF IN 718 subjected to standard solution annealing at 1065 °C as well as solution annealing followed by double-aging treatments (720 °C 8 h + 620 °C 8 h) using hole drilling test, correlating the resulting values with the microstructure evolution. In this study, subsequent heat treatments (solution annealing and aging treatments) provoked a consistent reduction of residual stresses.

Nevertheless, according to the authors' knowledge, there are no studies correlating the microstructure with residual stresses evolution under different temperatures, also applying temperatures considered as possible stress relieving tailored for the L-PBF material.

In the current work, a systematic study was performed in order to understand which temperature starts to be useful as stress relieving and which temperature starts to affect the microstructure of the material. Different heat treatments at 450, 600, 800, and 900 °C were compared to the as-built, and traditional solution annealed conditions at 980 °C (AMS 5662) and 1065 °C (AMS 5664) states, applying the same heating time (1 h). This study could drive to design specific heat treatments tailored for L-PBF IN 718 alloy to mitigate or eliminate the residual stresses.

## 2. Materials and Methods

### 2.1 Materials and Heat Treatments

The gas-atomized IN 718 powder supplied by EOS GmbH was used. The chemical composition is the following (in weight percent): Fe Balance, Ni 50–55%, Cr 17–21%, Nb 4.75–5.5%, Mo 2.8–3.3%, Co < 1%, Ti 0.65–1.15%, Al 0.2–0.8%, Si and Mn < 0.35%, Cu < 0.3%, P + S < 0.015% and B < 0.006% in agreement with the UNS N07718. The gas atomized powder was characterized by particles with a cumulative frequency of  $d_{50}$  of around 25  $\mu\text{m}$  and  $d_{90}$  of 45  $\mu\text{m}$ . The particle size was determined using processing images of the particles obtained by means of a scanning electron microscope (SEM). The particle presents quite spherical shapes, also exhibiting satellites and some irregular particles, as shown in Fig. 1.

Cubic samples with dimensions  $10 \times 10 \times 10 \text{ mm}^3$  were fabricated by means of an EOS M270 Dual mode version with a laser spot size of 0.1 mm. The employed process parameters were: laser power of 195 W, hatching distance of 0.09 mm, scanning speed of 1200 mm/s, and layer thickness of 0.02 mm, applying a laser scanning rotation of 67° (Ref 15). The employed scanning strategy has been explained in a previous publication of some of the authors (Ref 32).

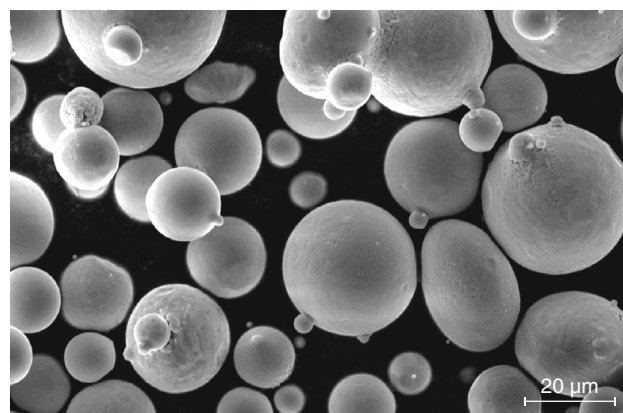


Fig. 1 SEM image of the morphology of the particles

In order to examine the residual stresses mitigation under heat treatments, different temperatures were selected. Heat treatments at 450, 600, 800, and 900 °C, together with standard solution annealing temperatures at 980 °C (AMS 5662) and 1065 °C (AMS 5664) were performed. For all these heat treatments, the heating time was kept constant to 1 h, followed by air cooling. The heat treatments were performed in a muffle furnace in air.

### 2.2 Microstructure Investigations

The cubic samples were cut along the z-axis (building direction), ground with SiC paper, and polished down to 1  $\mu\text{m}$  using diamond suspensions. Finally, the samples were etched with Kallings' No.2 solution. A light optical microscope (LOM - Leica DMI 5000 M) and scanning electron microscope (SEM - Phenom XL) equipped with an energy-dispersive spectroscopy (EDS) detector was employed to study the microstructure. The lattice parameter of the austenitic matrix ( $\gamma$ ) was evaluated by x-ray diffraction (XRD, PANalytical) with Cu K $\alpha$  radiation at 40 kV and 40 mA in a Bragg–Brentano configuration operating with a step size 0.013 and 25 s per step.

The Brinell hardness of the sample was determined using an EMCO TEST M4U test machine with a load of 62.5 kg $_f$  for 15 s (HBW2.5/62.5) following the ASTM E10 standard. The final hardness value was assessed by performing five indentations on two samples for each condition.

### 2.3 Residual Stresses Measurements

The hole-drilling method was used to evaluate the in-depth residual stresses. Thus, onto the top and lateral side of each specimen, K-RY61-1.5/120R (HBM Italia s.r.l., Italy) Type B3-element rosettes were installed. Each rosette consists of a series of 3 strain gages radially arranged to the point where the hole will be produced. A RESTAN-MTS3000 (SINT Technology s.r.l., Italy) hole drilling system, equipped with a 1.8 mm diameter inverted-cone end mill, was then used to generate the hole in 20 steps of 0.05 mm, and corresponding surface deformations were acquired. The EVAL 7 software (SINT Technology s.r.l., Italy) allowed to compute the residual stress profile from the acquired surface deformations, following the back calculation method for the non-uniform residual stress field described in the ASTM E837-13a standard.



### 3. Results and Discussions

#### 3.1 Microstructure Evolution

Figure 2 shows the LOM and SEM images of the as-built and heat-treated samples at 450 and 600 °C for 1 h, cut along the building direction (z-axis). The as-built state revealed the melt pool contours generated by the laser beam and columnar grains crossing several melt pools. Samples under thermal exposures at 450 and 600 °C displayed the same microstructure features as the as-built conditions. More in detail, the as-built state revealed columnar grains mainly with a length from 30 to 200  $\mu\text{m}$  and a width from 10 to 50  $\mu\text{m}$ , showing dimensions compatible with the literature (Ref 19, 22, 28). The grain size resulted in being no altered by applying heat treatments at 450 and 600 °C for 1 h. For these conditions, the SEM micrographs exhibited fine architectures of dendritic structures. This indicates that similar temperatures did not promote either melt pool disappearing or grains modifications or any significant phase changes.

Regarding the grain sizes, higher thermal exposures did not seem to involve drastic modification on the maximum grain dimensions due to the formation of phases hindering the grain growth. Moreover, all the microstructures exhibited the presence of columnar grains, indicating no remarkable recrystallization, as displayed in the LOM images of Fig. 3. This is in line with the literature on LPBF IN 718 alloy since the recrystallization primarily occurs over 1100 °C (Ref 15, 24).

Higher temperatures, on the other hand, produced detectable microstructural alterations on the melt pools, dendritic structures, and phases, as visible in the SEM micrographs of the specimens heat-treated at 800, 900, 980, and 1065 °C for 1 h in Fig. 3.

Heat treatment at 800 °C promoted the formation of precipitates along the grain boundaries, without eliminating the melt pools or affecting the columnar grains. Samples heat-treated at 900 °C still revealed precipitates along the columnar grain boundaries while the melt pools were almost completely eliminated, indicating that for this thermal exposure, dissolution mechanisms occur. Increasing the temperature at 980 °C, the microstructure still exhibited intergranular precipitates along the columnar grains while the melt pools were completely dissolved. Differently, the samples heat-treated at 1065 °C for 1 h revealed a very low concentration of phases along the grain boundaries.

The morphology and EDS analyses (Fig. 4a–d) associated with the time–temperature–transformation (TTT) diagram of the alloy can help to identify the formed phases under the various thermal exposures. Phases enriched in Nb coupled to depletion of Ni can suggest the formation of the carbides, while enrichment in Nb and Ni can indicate the formation of  $\delta$  phases ( $\text{Ni}_3\text{Nb}$ ). Moreover, considering that the austenitic matrix is already rich in Ni, for small  $\delta$  phases, the EDS analysis can also detect no Ni enrichment.

Heat treatment at 800 °C produced the formation of very fine carbides slightly enriched in Nb and depleted of Ni and Cr

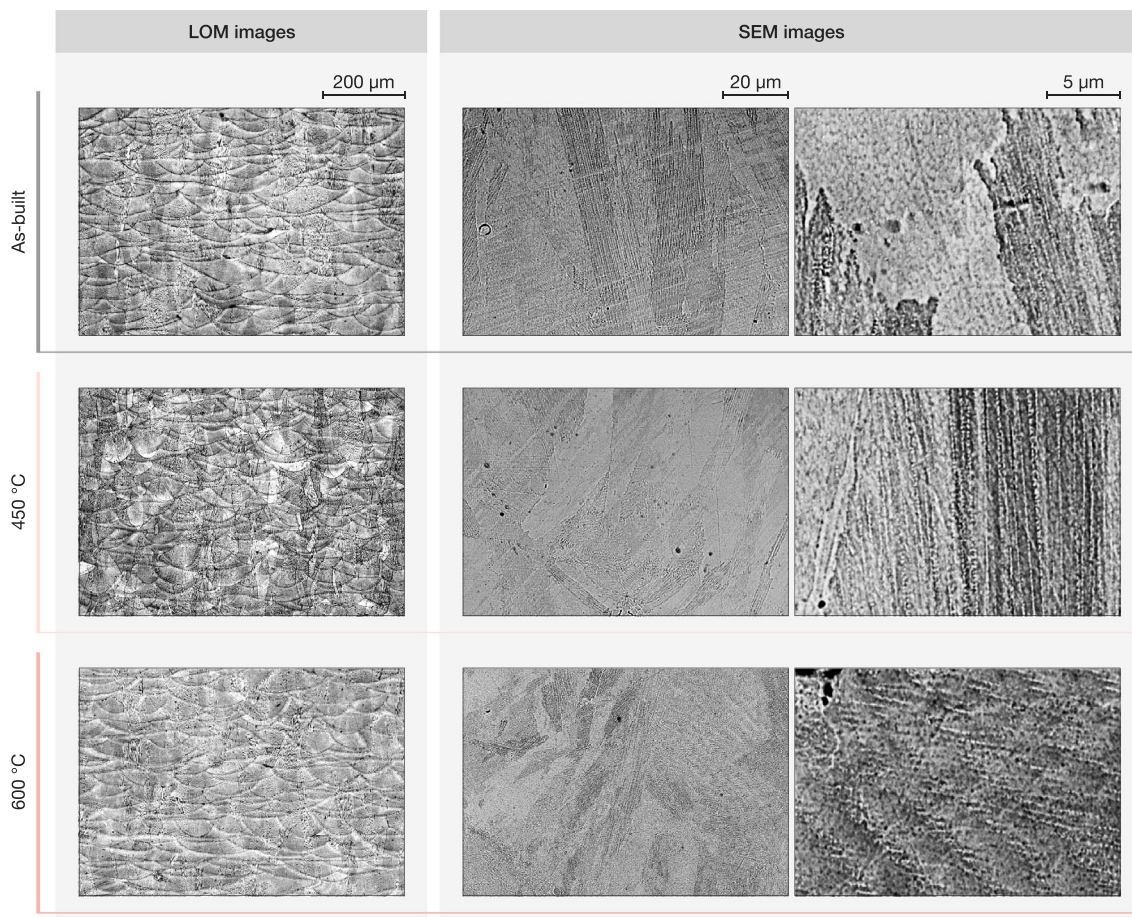


**Fig. 2** LOM and SEM images of the L-PBF Inconel 718 samples in the as-built state and heat-treated at 450 and 600 °C for 1 h. Kalling's No. 2 etchant was used

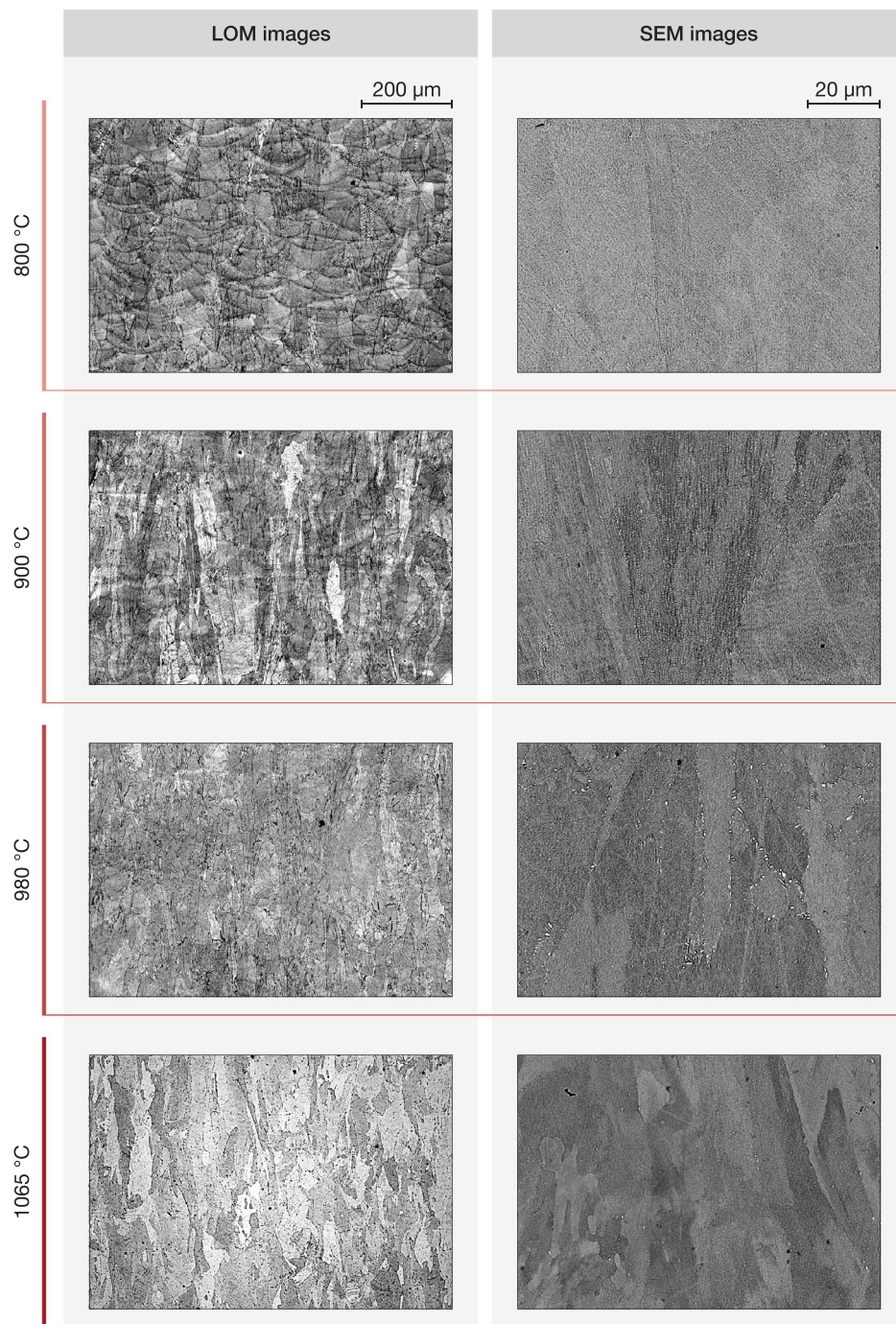


**Fig. 3** LOM and SEM images of L-PBF IN 718 samples heat-treated at 800, 900, 980, and 1065 °C for 1 h. Kalling's No.2 was used

along the grain boundaries. These carbides tend to be formed along these areas that are enriched in segregated chemical elements (C, Nb, etc.) (Ref 17, 21). Additionally, nanometric phases, such as  $\gamma''$  phases, could form based on the TTT curves of the alloy (Ref34).

After heat treatments at 900 and 980 °C, the microstructure revealed the formation of  $\delta$  phases both along the grain boundaries and inside the grains. The  $\delta$  phases of samples heat-treated at 900 and 980 °C exhibited enrichment in Nb and Ni (typical forming elements of this phase (Ref 12, 35). Inside the grains, the  $\delta$  phases tended to form predominately along with the interdendritic areas enriched in Nb. The

samples heat-treated at 980 °C exhibited coarser  $\delta$  phases than samples heat-treated 900 °C. The samples heat-treated at 980 °C revealed the presence of  $\delta$  phases from sub-micrometric to around 4  $\mu\text{m}$ , while the samples heat-treated at 900 °C mainly exhibited maximum dimensions up to around 2  $\mu\text{m}$ .

It should be noted that the distribution and dimension of  $\delta$  phases must be carefully controlled. This phase tends to increase the hardness, but its elevated concentration and dimensions can be detrimental to the ductility of the material. Moreover,  $\delta$  phases reduce Nb within austenitic matrix, which is essential for  $\gamma''$  phase formation during aging treatments



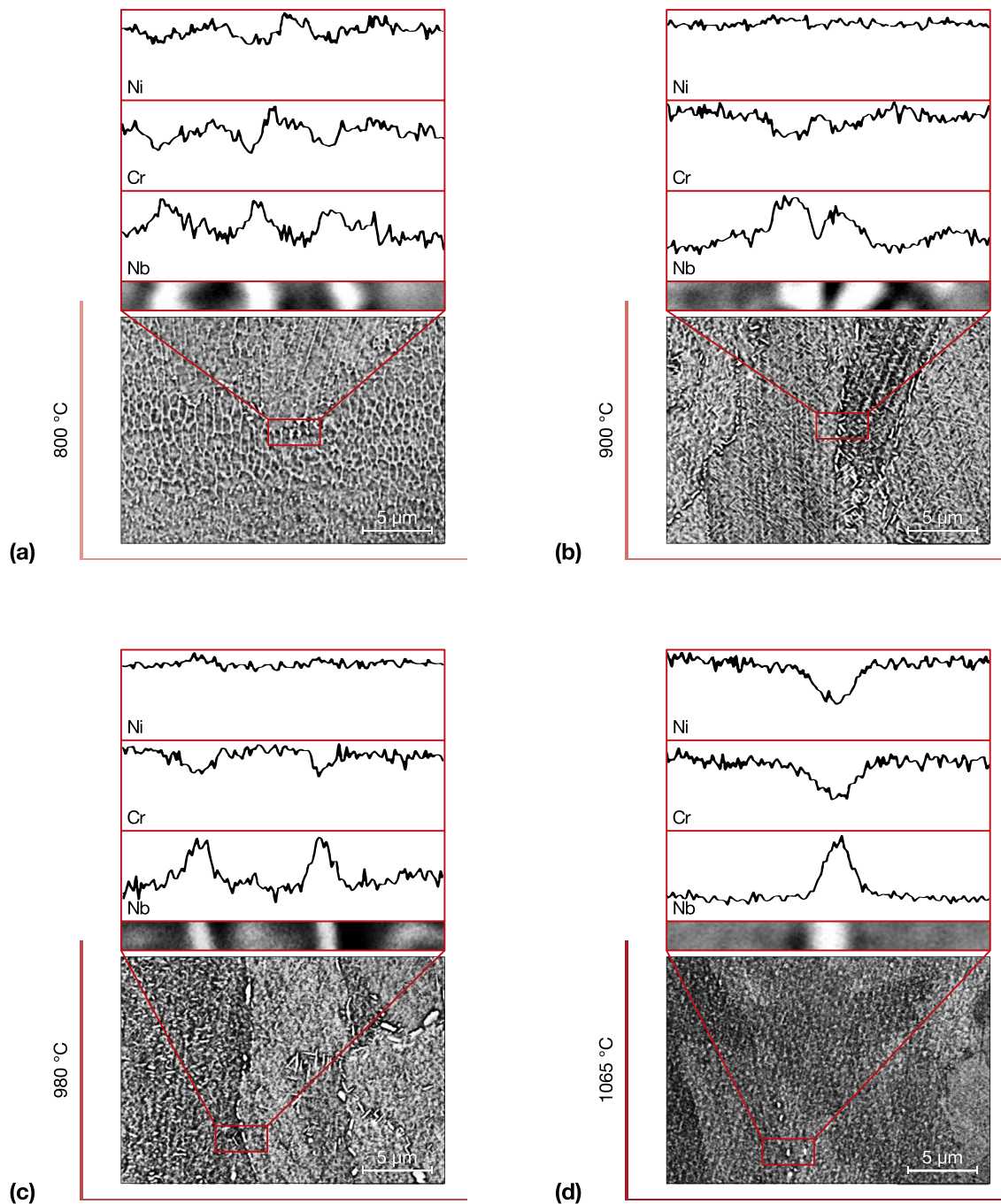


**Fig. 4** SEM images and EDS scan lines of the heat-treated IN 718 samples (a) 800, (b) 900, (c) 980, and (d) 1065 °C for 1 h. The EDS scan lines revealed the formation of carbides for samples heat-treated at 800 and 1065 °C and the formation of  $\delta$  phases for samples heat-treated at 900 and 980 °C

(Ref 2). From the microstructure analyses, 900 °C appeared to reduce the formation of large  $\delta$  phases.

A solution annealing at 1065 °C exhibited the complete dissolution of dendritic structures. The SEM images show the presence of intergranular carbides rich in Nb associated with the depletion of Ni and Cr with dimensions up to around 1  $\mu\text{m}$ .

### 3.2 XRD Analysis and Hardness Evolution

The microstructure development under heat treatments can be discussed employing the hardness and lattice parameter of  $\gamma$  phase. For Ni-based superalloys, it was reported that phase

formation could involve both an increment of the hardness and a reduction of the lattice parameters of the  $\gamma$  phase due to chemical elements depletion from the matrix. Differently, the dendritic dissolution can increase the lattice parameter of the  $\gamma$  phase (Ref 17, 36, 37).

For the as-built and heat-treated samples, the hardness and the lattice parameter of  $\gamma$  phase are displayed in Fig. 5(a) and (b), respectively.

The hardness and lattice parameter of  $\gamma$  phase of heat-treated samples at 450 and 600 °C resulted to be similar to the as-built ones, indicating no detectable modifications. On the other hand,

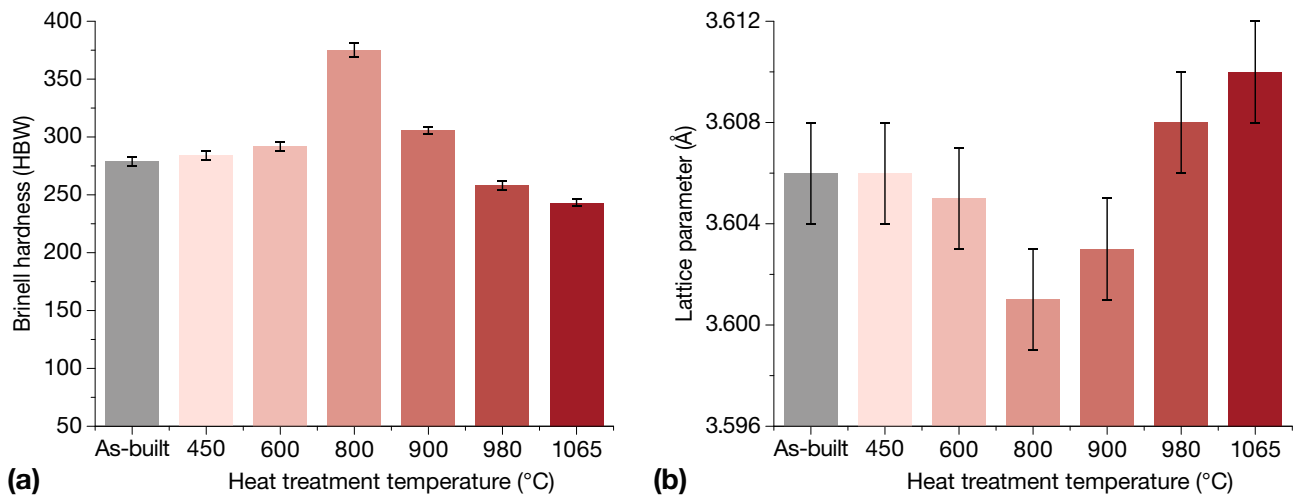


**Fig. 5** (a) Hardness of as-built and heat-treated samples at 450, 600, 800, 900, 980, and 1065 °C; (b) Lattice parameter of  $\gamma$  phase for the as-built and heat-treated samples at 450, 600, 800, 900, 980, and 1065 °C

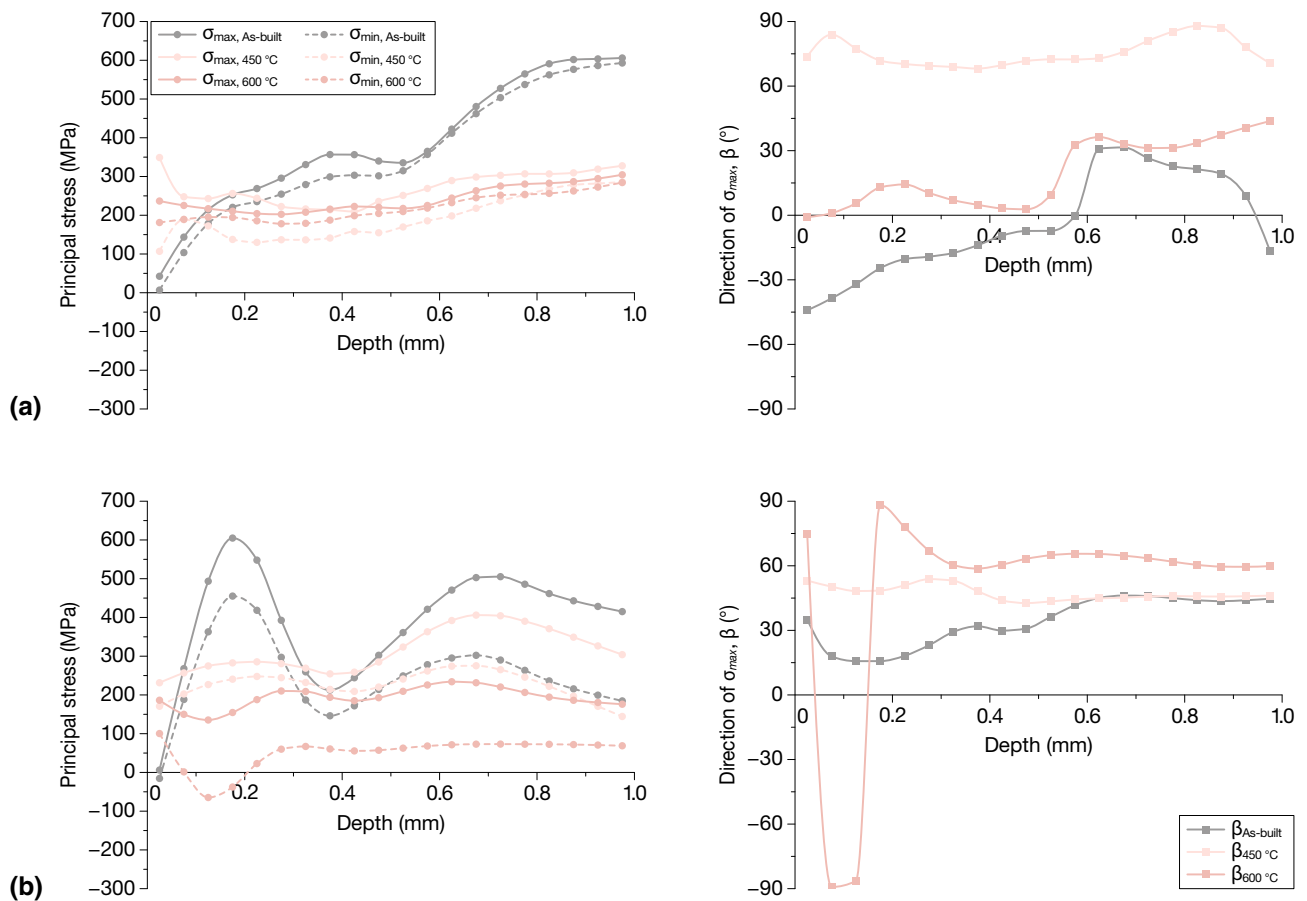


**Fig. 6** Residual stress profiles (a) on the top surface and (b) on the lateral side of the L-PBF IN 718 samples in the as-built state and heat-treated at 450 and 600 °C for 1 h

heat treatment at 800 °C involved a significant hardness increment coupled to lattice parameter reduction with respect to the as-built state. This was caused by the formation of carbides and more probably nanometric  $\gamma''$  phases, strengthening the material and reducing chemical elements from the matrix.

Samples heat-treated at 900 °C revealed higher hardness and slightly lower average lattice parameter than the as-built state. This can be attributed to the  $\delta$  phase formation.

The standard solution annealing at 980 °C revealed lower hardness and greater lattice parameter with respect to the as-built state. Even though the material presents a consistent

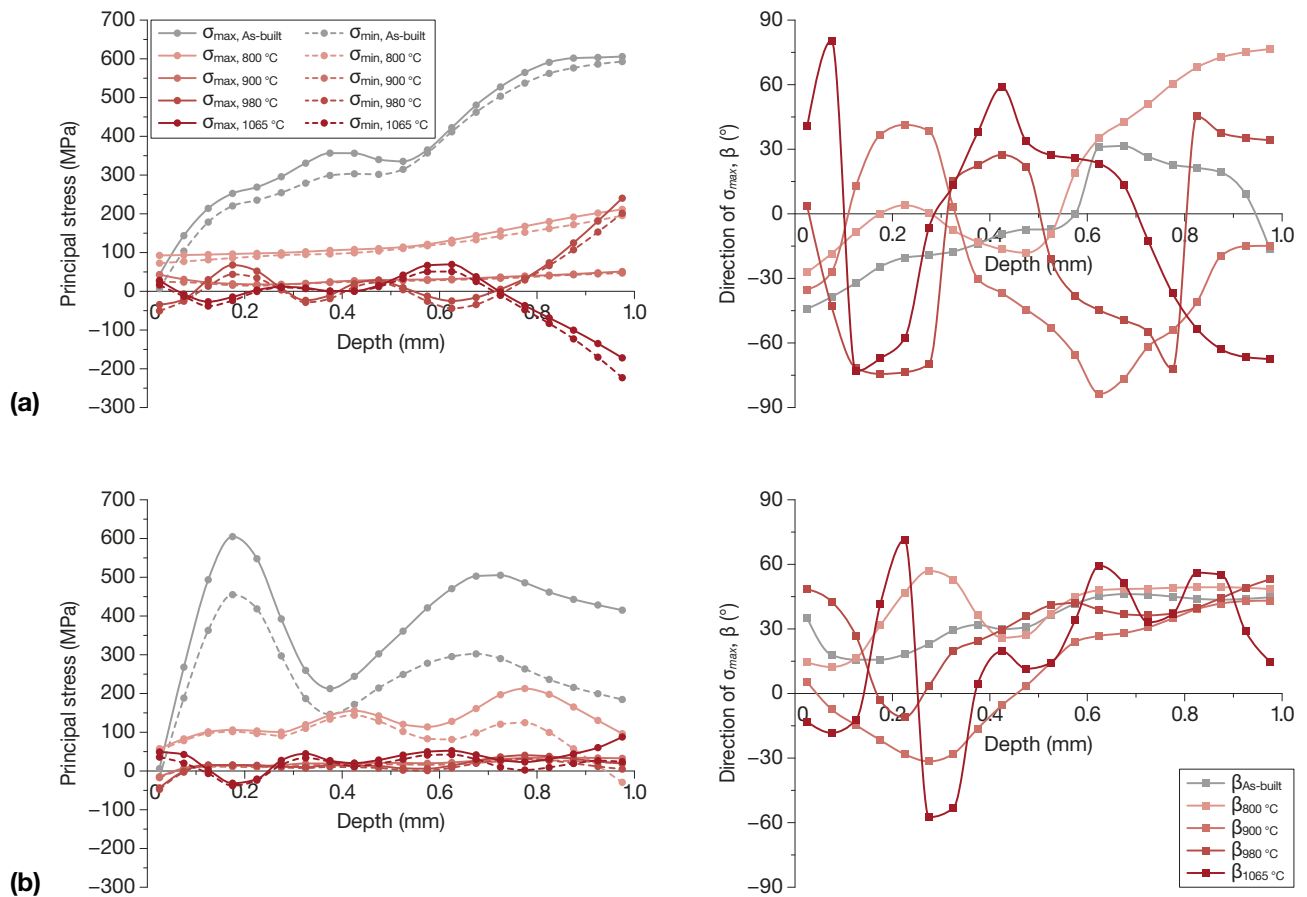


**Fig. 7** Residual stress profiles (a) on the top surface and (b) on the lateral side of the L-PBF IN 718 samples in the as-built state and heat-treated at 800, 900, 980, and 1065 °C for 1 h

quantity of  $\delta$  phases, the suppression of the melt pool structures and the partial dissolution of the dendritic structures lead to reduce the hardness and increase the lattice parameters.

The samples heat-treated at 1065 °C revealed the lowest hardness correlated with the highest lattice parameter. This derived from the complete suppression of melt pool structures and dendritic structures together with carbides formation occurred.

The hardness of the as-built and heat-treated samples at standard temperatures (980 and 1065 °C) are in good agreement with the literature using the hardness conversion of ASTM E140 (Ref 17).

### 3.3 Residual Stresses

The residual stresses for the as-built and different heat-treated IN 718 conditions along the top and lateral sides are reported in Fig. 6 and 7.

The as-built state showed the highest residual stress values, that were generated by the L-PBF process. Stresses were positive in sign, and on the top side maximum and minimum stresses were very close, indicating a biaxial tensile state. The stress profile below the top surface showed an initial increase from null stress to 250 MPa within the first 0.2 mm, then a moderate increase up to 350 MPa in the next 0.4 mm and finally a rapid rise to 600 MPa (almost reaching the yield strength of the as-built material built along the z-axis (Ref 38)

from a depth of 0.6 mm. According to ASTM E837 -13a standard, the uncertainty in stress value determination by the hole drilling method is on average  $\pm 10\%$ . Also, the direction of the principal stress showed an abrupt variation at a depth of 0.6 mm. Differently, the stress on the lateral surface was highest near the surface, reaching the maximum value of 600 MPa at 0.2 mm depth, and then oscillated between 200 and 500 MPa at higher depth.

The effectiveness of heat treatments at 450 and 600 °C on the reduction of residual stresses is clearly visible in Fig. 6. As concerns the top surface, quite uniform biaxial stresses of about 200 MPa were observed in both cases, with a moderate increase to 300 MPa only at higher depth. The maximum stress was around 45% of the yield stress of the material in the as-built state built along the z-axis (Ref 38). Different effects of the two heat treatments were instead observed on the lateral surfaces, and the somewhat oscillating stress still remained higher than 200 MPa after the heat treatment at 450 °C, whereas it was below 200 MPa when the higher temperature of 600 °C was adopted. This result suggests that the heat treatment at 600 °C is more effective in reducing the internal stresses.

A more remarkable residual stress reduction was obtained after the heat treatment at 800 °C (Fig. 7). After this treatment, the stress on the top side decreased to 100 MPa, with a slight increase to 200 MPa at higher depth. On the lateral side, the stress oscillated between 100 and 200 MPa.



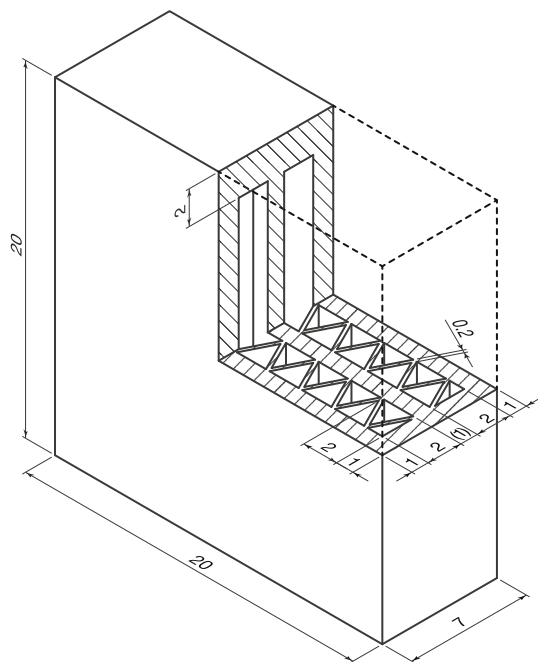


**Fig. 8** Geometry of the component with narrow internal channels (all dimensions in mm)

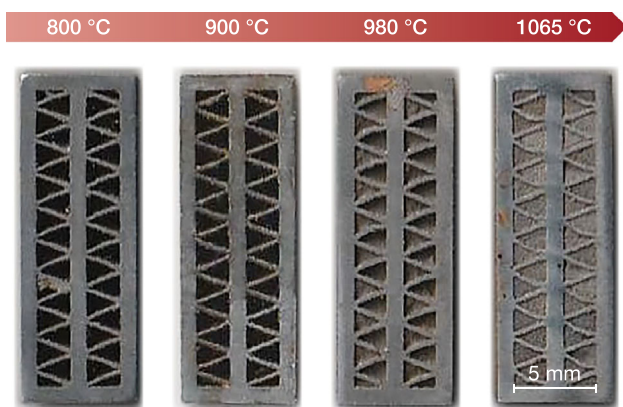


**Fig. 9** Components after cutting with narrow internal channels underwent to different heat treatments

On the other hand, heat treatment at 900, 980, and 1065 °C revealed the almost complete elimination of residual stresses (in this case the  $\beta$ -angle indication is not significant). The oscillating trends that were measured after the 980 and 1065 °C heat treatments, and that appeared amplified at higher depth may be ascribed to the formation of precipitate areas in the microstructure.

### 3.4 Components with Internal Channels

The investigated heat treatments were applied to components with narrow internal channels made of IN 718 by L-PBF. The geometry of these components is detailed in Fig. 8. After performing the heat treatments, the components were cut and checked if the powder was sintered within the narrow channels.

For heat treatments up to 900 °C for 1 h, the powder was not sintered within the internal channel. Differently, partial sintering of the powder occurred after heat treatments at 980

and 1065 °C for 1 h, entrapping the powder within the internal channels, as displayed in Fig. 9.

It is, therefore, evident that standard heat treatments could not be performed without before removing the powder from the internal channels. On the other hand, considering the current results, heat treatments at 800 and 900 °C could be performed to reduce the internal stresses without involving the sintering of the powder within the internal channels.

## 4. Conclusions

The influence of different heat treatments on the microstructure and residual stresses of L-PBF IN 718 alloy was investigated. The residual stresses within the material can lead to components distortions, making it necessary to perform a post-heat treatment. The current work revealed that:

- heat treatments at 450 and 600 °C for 1 h slightly reduced the residual stresses within the material, without providing consistent microstructure alterations with respect to the as-built state;
- higher temperatures resulted to be more effective in reducing the residual stresses, involving a different degree of microstructure modifications based on the temperature;
- heat treatment at 800 °C for 1 h produced consistent mitigation of the residual stresses, generating very fine phases composed of intergranular carbides and most likely nanometric  $\gamma''$  phases, drastically increasing the hardness of the samples;
- heat treatment at 900 °C for 1 h resulted to be effective in the suppression of residual stresses revealing the formation of  $\delta$  phases correlated with a slight increment of hardness compared to the as-built state;
- the standard solution-annealing temperatures at 980 and 1065 °C for 1 h eliminated the residual stresses but, at the same time, promoted significant dendritic dissolution correlated with hardness decrement. In particular, the samples heat-treated at 980 °C showed bigger  $\delta$  phases than samples heat-treated at 900 °C. The samples heat-treated at 1065 °C revealed the presence of intergranular carbides associated with a complete dissolution of dendritic structures.

Therefore, heat treatments performed at low temperatures with respect to the standard temperatures could be considered as tailored stress-relieving treatments for the L-PBF material, and consequently, decreasing distortions of the components generating a limited impact on the microstructure.

These heat treatments were also performed on components with narrow internal channels. For the standard heat treatments at 980 and 1065 °C, the powder was partially sintered within the channels. Differently, heat treatments at 800 and 900 °C could mitigate the residual stresses without triggering the initial sintering of the powder within the internal channels, which can be easily eliminated after removing the specimens from the building platform.

## Acknowledgments

The authors would like to acknowledge the European Horizon 2020 research and innovation programme; grant agreement

No.723795/4D Hybrid–Novel ALL-IN-ONE machines, robots, and systems for affordable, worldwide and lifetime distributed 3D hybrid manufacturing and repair operations. This work has been partially supported by “Ministero dell’Istruzione, dell’Università e della Ricerca” Award “TESHUN-83486178370409 finanziamento dipartimenti di eccellenza CAP. 1694 TIT. 232 ART. 6”. Moreover, the authors would like to acknowledge the Integrated Additive Manufacturing Centre at Politecnico di Torino (IAM@PoliTo) where the specimens were fabricated and characterized. Finally, the authors would like to thank Mr. Roberto Manzo for support in the preparation of samples during this research.

## Funding

Open access funding provided by Politecnico di Torino within the CRUI-CARE Agreement.

## Open Access

This article is licensed under a Creative Commons Attribution 4.0 International License, which permits use, sharing, adaptation, distribution and reproduction in any medium or format, as long as you give appropriate credit to the original author(s) and the source, provide a link to the Creative Commons licence, and indicate if changes were made. The images or other third party material in this article are included in the article’s Creative Commons licence, unless indicated otherwise in a credit line to the material. If material is not included in the article’s Creative Commons licence and your intended use is not permitted by statutory regulation or exceeds the permitted use, you will need to obtain permission directly from the copyright holder. To view a copy of this licence, visit <http://creativecommons.org/licenses/by/4.0/>.

## References

1. S.A. Nalawade, M. Sundararaman, J.B. Singh, A. Verma, and R. Kishore, Precipitation of  $\gamma'$  Phase in  $\delta$ -Precipitated Alloy 718 during Deformation at Elevated Temperatures, *Mater. Sci. Eng., A*, 2010, **527**(12), p 2906–2909. <https://doi.org/10.1016/j.msea.2010.01.006>
2. H. Zhang, C. Li, Q. Guo, Z. Ma, Y. Huang, H. Li, and Y. Liu, Hot Tensile Behavior of Cold-Rolled Inconel 718 Alloy at 650 °C: The Role of  $\delta$  Phase, *Mater. Sci. Eng., A*, 2018, **722**, p 136–146. <https://doi.org/10.1016/j.msea.2018.02.093>
3. A. Chamanfar, L. Sarrat, M. Jahazi, M. Asadi, A. Weck, and A.K. Koul, Microstructural Characteristics of Forged and Heat Treated Inconel-718 Disks, *Mater. Des.*, 2013, **52**, p 791–800. <https://doi.org/10.1016/j.matdes.2013.06.004>
4. L. Chang, W. Sun, Y. Cui, F. Zhang, and R. Yang, Effect of Heat Treatment on Microstructure and Mechanical Properties of the Hot-Isostatic-Pressed Inconel 718 Powder Compact, *J. Alloys Compd.*, 2014, **590**, p 227–232. <https://doi.org/10.1016/j.jallcom.2013.12.107>
5. H. Qi, M. Azer, and A. Ritter, Studies of Standard Heat Treatment Effects on Microstructure and Mechanical Properties of Laser Net Shape Manufactured INCONEL 718, *Metall. Mater. Trans. A Phys. Metall. Mater. Sci.*, 2009, **40**(10), p 2410–2422. <https://doi.org/10.1007/s11661-009-9949-3>
6. C.M. Kuo, Y.T. Yang, H.Y. Bor, C.N. Wei, and C.C. Tai, Aging Effects on the Microstructure and Creep Behavior of Inconel 718 Superalloy, *Mater. Sci. Eng., A*, 2009, **510–511**, p 289–294. <https://doi.org/10.1016/j.msea.2008.04.097>
7. C. Zhong, A. Gasser, J. Kittel, K. Wissenbach, and R. Poprawe, Improvement of Material Performance of Inconel 718 Formed by High Deposition-Rate Laser Metal Deposition, *Mater. Des.*, 2016, **98**, p 128–134. <https://doi.org/10.1016/j.matdes.2016.03.006>
8. D. Herzog, V. Seyda, E. Wycisk, and C. Emmelmann, Additive Manufacturing of Metals, *Acta Mater.*, 2016, **117**, p 371–392. <https://doi.org/10.1016/j.actamat.2016.07.019>
9. C.Y. Yap, C.K. Chua, Z.L. Dong, Z.H. Liu, D.Q. Zhang, L.E. Loh, and S.L. Sing, Review of Selective Laser Melting: materials and Applications, *Appl. Phys. Rev.*, 2015, **2**(4), p 1–22. <https://doi.org/10.1063/1.4935926>
10. W.E. King, A.T. Anderson, R.M. Ferencz, N.E. Hodge, C. Kamath, S.A. Khairallah, and A.M. Rubenchik, Laser Powder Bed Fusion Additive Manufacturing of Metals: Physics, Computational, and Materials Challenges, *Appl. Phys. Rev.*, 2015, **2**(4), p 041304. <https://doi.org/10.1063/1.4937809>
11. G. Marchese, E. Bassini, M. Calandri, E.P. Ambrosio, F. Calignano, M. Lorusso, D. Manfredi, M. Pavese, S. Biamino, and P. Fino, Microstructural Investigation of As-Fabricated and Heat-Treated Inconel 625 and Inconel 718 Fabricated by Direct Metal Laser Sintering: contribution of Politecnico Di Torino and Istituto Italiano Di Tecnologia (IIT) Di Torino, *Met. Powder Rep.*, 2016, **71**(4), p 273–278. <https://doi.org/10.1016/j.mprp.2016.06.002>
12. K. Moussaoui, W. Rubio, M. Mousseigne, T. Sultan, and F. Rezai, Effects of Selective Laser Melting Additive Manufacturing Parameters of Inconel 718 on Porosity, Microstructure and Mechanical Properties, *Mater. Sci. Eng. A*, 2018, **735**, p 182–190. <https://doi.org/10.1016/j.msea.2018.08.037>
13. Q. Jia and D. Gu, Selective Laser Melting Additive Manufacturing of Inconel 718 Superalloy Parts: densification, Microstructure and Properties, *J. Alloys Compd.*, 2014, **585**, p 713–721. <https://doi.org/10.1016/j.jallcom.2013.09.171>
14. L.N. Carter, X. Wang, N. Read, R. Khan, M. Aristizabal, K. Essa, and M.M. Attallah, Process Optimisation of Selective Laser Melting Using Energy Density Model for Nickel Based Superalloys, *Mater. Sci. Technol.*, 2016, **32**(7), p 657–661. <https://doi.org/10.1179/1743284715Y.0000000108>
15. M. Calandri, D. Manfredi, F. Calignano, E.P. Ambrosio, S. Biamino, R. Lupoi, and D. Ugues, Solution Treatment Study of Inconel 718 Produced by SLM Additive Technique in View of the Oxidation Resistance, *Adv. Eng. Mater.*, 2018, **20**(11), p 1800351. <https://doi.org/10.1002/adem.201800351>
16. Z. Wang, K. Guan, M. Gao, X. Li, X. Chen, and X. Zeng, The Microstructure and Mechanical Properties of Deposited-IN718 by Selective Laser Melting, *J. Alloys Compd.*, 2012, **513**, p 518–523. <https://doi.org/10.1016/j.jallcom.2011.10.107>
17. L. Zhou, A. Mehta, B. McWilliams, K. Cho, and Y. Sohn, Microstructure, Precipitates and Mechanical Properties of Powder Bed Fused Inconel 718 before and after Heat Treatment, *J. Mater. Sci. Technol.*, 2019, **35**(6), p 1153–1164. <https://doi.org/10.1016/j.jmst.2018.12.006>
18. J.L. Bartlett and X. Li, An Overview of Residual Stresses in Metal Powder Bed Fusion, *Addit. Manuf.*, 2019, **27**, p 131–149. <https://doi.org/10.1016/j.addma.2019.02.020>
19. M. Calandri, S. Yin, B. Aldwell, F. Calignano, R. Lupoi, and D. Ugues, Texture and Microstructural Features at Different Length Scales in Inconel 718 Produced by Selective Laser Melting, *Materials (Basel)*, 2019, **12**(8), p 1293. <https://doi.org/10.3390/ma12081293>
20. X. Wang and K. Chou, Effects of Thermal Cycles on the Microstructure Evolution of Inconel 718 during Selective Laser Melting Process, *Addit. Manuf.*, 2017, **18**, p 1–14. <https://doi.org/10.1016/j.addma.2017.08.016>
21. W.M. Tucho, P. Cuvillier, A. Sjolyst-Kverneland, and V. Hansen, Microstructure and Hardness Studies of Inconel 718 Manufactured by Selective Laser Melting before and after Solution Heat Treatment, *Mater. Sci. Eng., A*, 2016, **2017**(689), p 220–232. <https://doi.org/10.1016/j.msea.2017.02.062>
22. D. Zhang, Z. Feng, C. Wang, W. Wang, Z. Liu, and W. Niu, Comparison of Microstructures and Mechanical Properties of Inconel 718 Alloy Processed by Selective Laser Melting and Casting, *Mater. Sci. Eng., A*, 2018, **724**(100), p 357–367. <https://doi.org/10.1016/j.msea.2018.03.073>
23. G.H. Cao, T.Y. Sun, C.H. Wang, X. Li, M. Liu, Z.X. Zhang, P.F. Hu, A.M. Russell, R. Schneider, D. Gerthsen, Z.J. Zhou, C.P. Li, and G.F. Chen, Investigations of  $\gamma'$ ,  $\gamma''$  and  $\delta$  precipitates in heat-treated Inconel 718 alloy fabricated by selective laser melting, *Mater. Charact.*, 2018, **136**, p 398–406. <https://doi.org/10.1016/j.matchar.2018.01.006>
24. E. Chlebus, K. Gruber, B. Kuźnicka, J. Kurzac, and T. Kurzynowski, Effect of Heat Treatment on the Microstructure and Mechanical Properties of Inconel 718 Processed by Selective Laser Melting, *Mater.*

- Sci. Eng., A*, 2015, **639**, p 647–655. <https://doi.org/10.1016/j.msea.2015.05.035>
25. A. Salmi and E. Atzeni, Residual Stress Analysis of Thin AlSi10Mg Parts Produced by Laser Powder Bed Fusion, *Virtual Phys. Prototyp.*, 2020, **15**(1), p 49–61. <https://doi.org/10.1080/17452759.2019.1650237>
  26. A. Salmi and E. Atzeni, History of Residual Stresses during the Production Phases of AlSi10Mg Parts Processed by Powder Bed Additive Manufacturing Technology, *Virtual Phys. Prototyp.*, 2017, **12**(2), p 153–160. <https://doi.org/10.1080/17452759.2017.1310439>
  27. N.C. Levkulich, S.L. Semiatin, J.E. Gockel, J.R. Middendorf, A.T. DeWald, and N.W. Klingbeil, The Effect of Process Parameters on Residual Stress Evolution and Distortion in the Laser Powder Bed Fusion of Ti-6Al-4 V, *Addit. Manuf.*, 2019, **28**, p 475–484. <https://doi.org/10.1016/j.addma.2019.05.015>
  28. J.H. Yi, J.W. Kang, T.J. Wang, X. Wang, Y.Y. Hu, T. Feng, Y.L. Feng, and P.Y. Wu, Effect of Laser Energy Density on the Microstructure, Mechanical Properties, and Deformation of Inconel 718 Samples Fabricated by Selective Laser Melting, *J. Alloys Compd.*, 2019, **786**, p 481–488. <https://doi.org/10.1016/j.jallcom.2019.01.377>
  29. Y. Lu, S. Wu, Y. Gan, T. Huang, C. Yang, L. Junjie, and J. Lin, Study on the Microstructure, Mechanical Property and Residual Stress of SLM Inconel-718 Alloy Manufactured by Differing Island Scanning Strategy, *Opt. Laser Technol.*, 2015, **75**, p 197–206. <https://doi.org/10.1016/j.optlastec.2015.07.009>
  30. D. Deng, R.L. Peng, H. Brodin, and J. Moverare, Microstructure and Mechanical Properties of Inconel 718 Produced by Selective Laser Melting: sample Orientation Dependence and Effects of Post Heat Treatments, *Mater. Sci. Eng., A*, 2018, **713**, p 294–306. <https://doi.org/10.1016/j.msea.2017.12.043>
  31. N. Nadammal, S. Cabeza, T. Mishurova, T. Thiede, A. Kromm, C. Seyfert, L. Farahbod, C. Haberland, J.A. Schneider, P.D. Portella, and G. Bruno, Effect of Hatch Length on the Development of Microstructure, Texture and Residual Stresses in Selective Laser Melted Superalloy Inconel 718, *Mater. Des.*, 2017, **134**, p 139–150. <https://doi.org/10.1016/j.matdes.2017.08.049>
  32. R. Barros, F.J.G. Silva, R.M. Gouveia, A. Saboori, G. Marchese, S. Biamino, A. Salmi, and E. Atzeni, Laser Powder Bed Fusion of Inconel 718: residual Stress Analysis Before and After Heat Treatment, *Metals (Basel)*, 2019, **9**, p 1290. <https://doi.org/10.3390/met9121290>
  33. B. Ahmad, S.O. van der Veen, M.E. Fitzpatrick, and H. Guo, Residual Stress Evaluation in Selective-Laser-Melting Additively Manufactured Titanium (Ti-6Al-4V) and Inconel 718 Using the Contour Method and Numerical Simulation, *Addit. Manuf.*, 2018, **22**, p 571–582. <https://doi.org/10.1016/j.addma.2018.06.002>
  34. H. Chandler, Ed., *Heat Treater's Guide: Practices and Procedures for Nonferrous Alloys*, Materials Park, ASM International, 1996
  35. M.J. Donachie and S.J. Donachie, *Superalloys: A Technical Guide*, 2nd ed., Materials Park, ASM International, 2002
  36. G. Marchese, S. Parizia, M. Rashidi, A. Saboori, D. Manfredi, D. Ugues, M. Lombardi, E. Hryha, and S. Biamino, The Role of Texturing and Microstructure Evolution on the Tensile Behavior of Heat-Treated Inconel 625 Produced via Laser Powder Bed Fusion, *Mater. Sci. Eng., A*, 2020, **769**, p 138500. <https://doi.org/10.1016/j.msea.2019.138500>
  37. S. Li, Q. Wei, Y. Shi, Z. Zhu, and D. Zhang, Microstructure Characteristics of Inconel 625 Superalloy Manufactured by Selective Laser Melting, *J. Mater. Sci. Technol.*, 2015, **31**(9), p 946–952. <https://doi.org/10.1016/j.jmst.2014.09.020>
  38. EOS NickelAlloy IN718 (Datasheet). Available Online: 2020. <https://www.eos.info/en/additive-manufacturing/3d-printing-metal/dmls-metal-materials/nickel-alloys>. Accessed 20 May 2020

**Publisher's Note** Springer Nature remains neutral with regard to jurisdictional claims in published maps and institutional affiliations.